Active Site Engineering via Optimizing Heterogeneous Support Structure for Single Atom Catalysis

Suming An¹, Prajay Patel^{2, 3}, Cong Liu*², and Rex T. Skodje*¹

- 1) Department of Chemistry, University of Colorado, Boulder, CO 80309
- 2) Chemical Sciences and Engineering Division, Argonne National Laboratory, Lemont,

IL 60639

3) Department of Chemistry, University of Dallas, Irving, TX, 75062

Abstract: Supported single-atom catalysts (SAC) show a large range of activity and selectivity that depend on the local environment of the catalytic sites. A theory-based optimization strategy is presented that is based on a density functional theory (DFT) determination of the transition states and intermediates for a low-dimensional coordinate representation of the heterogeneity of the active sites. The approach is applied to a vanadium catalyst on an amorphous SiO₂ support that involves a large kinetic network described using a full-chemistry model. Without assuming a priori scaling relations or mechanism reduction, the optimal state of heterogeneity is found to lie at atomic configurations where the activation energies for two distinct key chemical processes are equal. It is found a posteriori that the behavior of the system is consistent with linear free energy scaling relations in the randomness parameters. The energetic span theory proves quite useful in reducing the full chemistry model to a small number of key reactions. The use of a nonlinear optimization algorithm in combination with energetic span theory provides significant simplification in treating disordered systems.

Corresponding Authors:

Rex T. Skodje – orcid.org/0000-0003-1601-5189; Email: rex.skodje@colorado.edu.

Cong Liu – orcid.org/0000-0002-2145-5034; Email: congliu@anl.gov.

1.Introduction

The design of optimal catalysts to promote a chemical process is a long-standing objective in chemistry and engineering. In the optimization paradigm, a desirable quantity such as the turnover frequency (TOF), product selectivity, or energy release is maximized with respect to a set of controllable parameters that constitute the design space. This design space may include the identity of a catalytic metal or alloy, the ligands attached to the active site, the pH or temperature of the reactor, among many other possible choices. The range of these features is restricted to a feasible set (FS) of physically reasonable values. With the advances occurring in the efficiency of computational chemistry, it has become increasingly possible to use ab initio methods to determine the design variables which optimize performance over a family of catalysts. 1 2 3 4 5 6 This approach can produce a so-called "volcano plot" where the predicted activity or other desired quantity shows a sharp maximum as a computational input is varied.^{78 9 10} Often a key descriptor is the binding energy of an intermediate adsorbate species along the chemical pathway which then can be used to screen large numbers of candidate catalysts. Optimization packages are now available for a wide variety of important catalytic systems and numerous strategies exist that often employ machine learning methodology. 11 12 13 14 One design variable that is difficult to model is the disorder of the catalytic environment, i.e., the heterogeneity of the catalytically active site. The active site heterogeneity may reflect the conformational structure of an enzyme, the random distribution of adsorbates on a metallic surface, or, as in the present case, the anchoring (or grafting) site of a catalytic atom on an amorphous support. Despite clear evidence that local environment surrounding the active site strongly influences activity, it has proven difficult to quantitatively characterize such randomness in a systematic way. The direct observation of chemistry at individual active sites using traditional methods of surface science is obscured since measurements tend to average over atomic environments. Recent studies suggest, however, that spatially resolved atomic level (scanning tunneling microscopy) STM or (scanning transmission electron microscopy) STEM measurements, in tandem with theoretical modeling, can provide considerable insight in the nature of single-atom catalysts (SAC).¹⁵ In principle, single molecule kinetics also provides an experimental window into the role of atomic level disorder revealed in real time. 17 18 19 ²⁰ For most catalytic systems of interest, however, such experiments are not currently feasible and we rely mostly on theoretical modeling for insight.

The atomic state of disorder may change with time. As an umbrella concept, we note that molecular disorder experienced by the catalyst can be characterized by the time scale that quantifies the passage between disordered states.²¹ For static disorder, the time scale is extremely long, and the catalyst is essentially frozen in place during the course of the experiment. For dynamic disorder, such as with enzymatic catalysis or dynamic fluxionality of high temperature metal clusters²², the catalyst activity is fluctuating at an observable rate that may even be comparable to the TOF. Here we focus on static disorder, where the rate coefficients for the catalytic network are time-independent at each individual catalytic site in the sample. We further specialize the methods to cases of grafted SAC on an amorphous support which is illustrated here using an explicit model of an olefin hydrogenation reaction using a vanadium catalyst on silica.

There are an enormous number of distinct grafting sites available to the vanadium complex each of which is characterized by a different effective activity. This discrete distribution of catalytic environments is labeled by the high-dimensional coordinate vector, X, describing the relaxed equilibrium atomic structure. It is difficult to optimize the TOF versus X since each structure is an isolated minimum of the energy function that ideally should be separately sought and then kinetically modeled. Instead, we shall pursue an approach based on an approximate continuum model of the where it is assumed that X can be described as a continuous variable which labels various potential SAC environments. This allows the use of powerful optimization methods that can efficiently search the high-dimensional space of disordered states. It is approximate in that the values of X explored in the search are not fully relaxed states. However, the approximate optimization does reveal zones of high activity and provides clues as to the design targets.

The disordered state is assumed to be parameterized by a small subset of the atomic structures, $x \subset X$, describing the local environment of the active site, such as bond lengths and angles of the spectator atoms surrounding the SAC. The activity of the state x is determined using ab initio methods where the remaining coordinates in X are then fully relaxed. This short-ranged disorder can be supplemented, if necessary, with much weaker additive Gaussian noise to represent long-ranged randomness. The catalytic sample is represented by a probability distribution of these environments. If the local coordinates, x, are held fixed to represent a single catalytic environment in the distribution, the energetics of the network of chemical reactions $\{G(x)\}$ occurring at the active site can be obtained from quantum mechanical (QM) calculations, where x are treated as fixed constraints and $\{G(x)\}$ represents the free energies of the intermediates (INT) and transition

states (TS). Since the rate coefficients of the network $\{k(x)\}$ can be computed using transition state theory (TST), it is then possible to construct kinetic observables as explicit functions of x to obtain, e.g., an activity map vs. x. Likewise, a selectivity map can be created from the kinetics when chemically branched pathways exist. When numerical optimization methods are applied to those observables, the most effective disordered environments x^* can be discovered as illustrated by the simple scheme

$$x \xrightarrow{QM} \{G(x)\} \xrightarrow{TST} \{k(x)\} \xrightarrow{Activity Map(x)} \xrightarrow{x^*(TOF)} Selectivity Map(x) \xrightarrow{x^*(Select)} kinetics optimization$$

It then becomes a problem in synthesis to fashion ways in which those environments may be enhanced in creating a sample. The regions of high activity or selectivity correspond to hotspots on the sample where greater turnovers of a given product are seen. The potential for direct observation of such hotspots was demonstrated by Chen and coworkers²³ via mapping the site-specific chemistry on two-dimensional nanocrystals.

The practical challenges of theoretically designing optimally disordered environments are significant. In addition to the need to develop a cogent and effective optimization formalism, the computations must necessarily involve many QM evaluations at a sufficiently high-level accuracy for a large number of environments. This burden is compounded since the chemical mechanism itself may involve many reactions and intermediates. Thus, if N_d disordered environments need to be sampled for N_s chemical states, we then would require $N_d \times N_s$ large QM calculations. We can reduce this daunting number in two ways. First, by the process of mechanism reduction, the chemistry can be reduced to a smaller number of key kinetic steps. This greatly lessens the number of chemical structure determinations needed and has been extensively used in many applications. In the most extreme form, this might constitute a reduction to a single reaction. Second, using efficient numerical optimization algorithms the disorder space can be searched to find regions of optimal performance thus avoiding the need to engage in a systematic sampling of the space.²⁴ ²⁵

In the present work, we propose an optimization method that is adaptable to a variety of disordered systems where single point QM calculations are feasible for the relevant chemical structures. The methods proposed build on a kinetic model we have recently developed which has

been shown to account for many aspects of the observed kinetics of the vanadium SAC.²⁶ ²⁷ ²⁸ The nonlinear optimization method can then identify disordered states that maximize a desired feature using either a full chemistry model or a reduced model. We consider a vanadium based SAC on an amorphous support that catalyzes an alkene hydrogenation reaction. The previous microkinetic model is extended to a larger disorder space with more extensive calculations. The results were analyzed using a novel spectral technique to understand the physical basis behind the optimization. The role of linear scaling relationships in the disorder variables is then discussed.

2. Theoretical Methods

A. The Microkinetic Model and Energetics

The disorder in the present problem results from the underlying amorphous support which has been characterized extensively. Experimentally, there are multiple reported values for Si-O bond distances and angles.²⁹ ³⁰ ³¹ Computationally, Ewing et al.³² and Fogerty el al.³³ outlined methods to generate amorphous silica models that are consistent with experimental bulk properties like density and Si-O bond distances and angles. Grafting sites on amorphous silica are characterized by the presence of silanol groups on the surface and the podality (e.g., bipodal or tripodal grafting sites) is dictated by the distance between two silanol groups, which can be represented by the Euclidean distance between the two O atoms of the silanol groups. Using these computational models³² ³³ reveals how hydroxylated amorphous silica surface models will generate a distribution of O-O distances for potential bipodal and tripodal grafting sites. In Fig. 1, we show a sample structure obtained using classical molecular dynamics and DFT. Using an annealing process with the ReaxFF followed with DFT geometries, a series of structures a can be generated that represent potential grafting sites. These are distributed as shown in on the right side of Fig. 1. This distribution is broad and consistent with the idea that the catalytic environments may be modeled using a continuous range of short-ranged coordinate parameterizations. Also note that the podality contributes to the rigidity/flexibility of the single atom catalyst,³⁴ which has an impact on catalysis as shown in previous work where a grid-like scan of the distribution of potential grafting environments of a silica-supported organovanadium(III) catalyst was used to model styrene hydrogenation kinetics.²⁶ ²⁷ ²⁸ There, it was shown that the computed kinetics were qualitatively consistent with experimental kinetic measurements using combinations of different grid points, i.e., a combination of contributing environments. Thus, it was emphasized that multiple disordered

environments were required to explain the observed pathway switching between distinct chemical paths. Other computational approaches include a quenched disorder model with reinforcement learning, which indicated that individual active sites contribute to a distribution of activation barriers for single-atom catalysis.^{35 36 37} We emphasize that all tractable computational models will show some loss of realism for amorphous silica-supported single atom catalysts, but they nevertheless show how incorporating a few design variables effectively characterize key aspects of the kinetics of catalysis.

We specifically consider the optimization of a SAC that is anchored to amorphous silica. Due to the variation in chemical activation barriers of the chemical network, catalytic activities will form a distribution over the grafting sites. We seek the most active sites in that distribution. The organometallic vanadium(III) compound modeled catalyzes the hydrogenation of an alkene substrate in a nonpolar solution phase. The synthesis involves the creation of a (SiO₂)vanadium(III)mesityl(MES)tetrahydrofurane(THF) pre-catalyst shown in Fig. 2a. In laboratory experiments, the pre-catalyst is activated by prolonged exposure to hydrogen that strips away the MES ligand.³⁸ The THF species is part of the pre-catalytic structure and plays the role of an inhibitor when present in the bulk solution. The chemistry modeled here is styrene (ST) hydrogenation to form ethyl benzene. The catalytic chemistry of butyl styrene and other similar alkene hydrogenation reactions have been extensively studied in the laboratory using traditional kinetic methods and using structural characterizations employing X-ray absorption near edge structure (XANES) spectroscopy. 39 Based on these findings, a microkinetic model has been proposed that accounts for the hydrogenation process which involves three interconverting active sites and three coupled catalytic cycles.²⁶ ²⁷ ²⁸ ⁴⁰ The proposed microkinetic model, represented in Fig. 2c, presumes the dominance of a heterolytic cleavage mechanism involving a tripodal vanadium active site. Three chemically distinct chemical pathways are possible that differ in the participation of the THF species and the ordering of the H₂ or ST addition; these are labeled as paths 5, 6, and 7 in Fig. 2c. Under most circumstances path 7 dominates the kinetics although, at high levels of [THF] inhibition and for certain grafting sites, the relative flux along path 5 becomes higher than either path 6 or 7. This microkinetic model, which emphasizes the heterolytic cleavage mechanism, is in agreement with the experimentally observed³⁹ behavior of the TOF with respect to $[H_2]$, [ST], and [THF].

The disorder observed in this system is a manifestation of a range of potential anchoring sites available to the catalytic precursor on the amorphous silica. In principle, the ab initio prediction of the distribution of vanadium anchoring sites would require a molecular level representation of the silica support followed by modeling of the synthetic chemistry leading to the pre-catalyst. Progress in this direction for similar systems have been made by Peters and coworkers using a quenched disorder model for the support.³⁶ ³⁷ However, rather than pursuing an ab initio prediction for a particular choice of disordered sample, we attempt to map out the activity of potential anchoring sites as a function of the disorder parameters which then provide targets for synthetic strategies. In order to understand the guiding issues, we investigate two-dimensional and three-dimensional representations of the disorder where the exhaustive computation of the energetics and kinetics are still possible. In this approach, the disorder coordinates x are fixed and the optimized barriers and wells of the reaction network are computed. For the two-dimensional case, x are chosen as the V-O and O-O bond lengths, see Fig. 2a. In the three-dimensional case, x are taken as the three O-O bonds of the silica support which surround the anchoring site of the Vatom, see Fig. 2b. Each value of x, either (r_{OO}, r_{VO}) or (r_1, r_2, r_3) , represents a possible catalytic site created in a synthetic process with some probabilistic weighting. These choices were made based on the sensitivity of the observed QM energetics to the variation of various configurations.

The *ab initio* free energies were calculated on discrete grids of these disorder variables, which are held fixed in the geometry optimization. A continuous representation was obtained using numerical interpolation. The calculations were done using a cluster model with density functional theory (DFT) implemented with the Gaussian 16 package.⁴¹ The geometry optimization was done using the B3LYP^{42 43} density functional and the CEP-31G^{44 45 46} pseudopotential double-ζ basis set in the gas phase. The lower half of the silica cage model (6 H, 11 O, and 6 Si atoms) was kept frozen during all the geometry optimization calculations as were the values of the disorder coordinates. The standard free energy for each of the 13 structures of Fig. 2c, including the precatalytic structure, was computed at 323.15° K consistent with experimental conditions³⁹39 using the B3LYP functional with the TZVP⁴⁷ basis set. Further details on the DFT calculations have been given previously²⁶ but here have been extended to expanded models of disorder.

For the 2D model, a grid of 35 values of the coordinates $\mathbf{x} = (r_{VO}, r_{OO})$. These two bond distances are defined in Fig. 2a. The full cluster geometries were generated by constraining the bond distances of r_{VO} and r_{OO} at grid values and optimizing the remaining active coordinates. The

standard free energies were computed for each structure shown in Fig. 2c. The bond distances chosen for r_{VO} were 2.1, 2.2, 2.3, 2.4, and 2.5 Å, which were considered based on their effect on the catalytic activity²⁶. The bond distances chosen for r_{OO} were 2.5, 2.7, 3.0, 3.3, 3.6, 3.9, and 4.2 Å, which were based on the physical constraints on the silica surface due to the surface strain of potential grafting sites. Since the grid is uniform, we employed a two-dimensional cubic spline interpolation scheme to evaluate energies at arbitrary values of (r_{VO},r_{OO}). The energies of all barriers and wells of the reaction network and the pre-catalyst are given in Table S1 in the supporting information (SI).

For the 3D representation of disorder, we use the three coordinates r_1 , r_2 , and r_3 which label the distance between the vanadium atom and the three closest oxygen atoms of the silica support. These coordinates are depicted in Fig. 2b. The key structures to the kinetics were identified by sensitivity analysis as the active site D, the barriers 23 and 25, and the intermediate well 24. The free energies for these structures were obtained on a grid of 75 values of the (r_1,r_2,r_3) coordinates. No symmetries were assumed in the (r_1,r_2,r_3) space. The free energies at 323.15° K for the four key kinetic structures and of the pre-catalyst are given in Table S2 of the SI. The grid is not uniform since a number of points were discarded that did not show adequate stability of the quantum calculation. Therefore, a radial basis set interpolation scheme was used. The Hessians corresponding to the B3LYP/TZVP calculations are extracted from Gaussian formatted checkpoint files. The Hessian can be transformed between coordinate systems using the chain rule.

B. Kinetic Modeling

The free energies of structures shown in Fig. 2c are used to determine the kinetics in x-space, where each point x represents a potential SAC in the sample. The rate coefficient for each elementary step $j \leftarrow i$ in the catalytic network is given by the Eyring form

$$k_{i,j}(\mathbf{x}) = \frac{k_B T}{h} \cdot exp\left(-\frac{\Delta G_a^{0,(j \leftarrow i)}(\mathbf{x})}{k_B T}\right) [Z] \tag{1}$$

where $\Delta G_a^{0,(j \leftarrow i)}(\mathbf{x})$ is the standard free energy of activation and [Z] is the substrate concentration for any additional reactant. The indices refer to any intermediate or active site (AS). The steady state kinetics can then be derived from the pseudo-first-order rate matrix

$$K(x) = \begin{pmatrix} -k_1(x) & \dots & k_{1,N+1}(x) \\ \vdots & \ddots & \vdots \\ k_{N+1,1}(x) & \dots & -k_{N+1}(x) \end{pmatrix}$$
(2)

where the diagonal elements of K(x) are the species decay rates $k_i(x) = \sum_{j \neq i} k_{j,i}(x)$ and thus column sum of K(x) is zero. N is the number of distinct states of the SAC and N+1 index occurs since both the reactant and product states of the AS are included in K. Following the methods introduced in ref. 28 the population of each molecular species involving the vanadium atom is described by a state i with a probability P_i . The normalization condition $\sum P_i = 1$ enforces the conservation of catalyst. The kinetics for the reaction network is described by three coupled catalytic cycles and three interconverting AS shown in Fig. 2c. For simplicity, we focus on the initial rates when the product concentration is zero. The steady state properties are found using an efficient linear algebra method based on a Markov state model interpretation of the catalytic chemistry. This analysis employs the N×N state-to-state transition matrix T(x), which is identical to -K(x) except the product forming reactions are omitted. The exact initial TOF, derived in ref. 28, gives a TOF

$$\nu(x) = \frac{1}{\mathbf{1}^T \cdot \left(-T(x)\right)^{-1} \cdot P_0} \tag{3}$$

In eq. 3, P_0 is the vector representing the steady state distribution of AS only and I is a vector of all 1's. The AS are the states formed upon product formation. This applies even when the resting state is not an AS. Often P_0 is just $(1,0,0,...)^T$ corresponding to a single AS. Equation 3 is completely equivalent to steady state solution of the conventional mass action equations for [Product]=0 but can be carried out without time evolution or imposing conservation constraints.

At temperatures below about 400° K and for certain values of x it is found that the T-matrix becomes ill-conditioned reflecting a huge separation of time scales between the chemical relaxation modes in the network. This leads to instability of the linear algebra. A regularization scheme is proposed in Sec. S3 of the SI which extrapolates the stable results from higher temperature to the lower experimentally reasonable temperature of 323.15° K.

C. Reduced Mechanism

To reduce the number of structures for QM calculation, we employ a novel mechanism reduction scheme which is tested the against full chemistry model. The difficulty with the disorder

problem is that the rate-limiting reactions can change as a function of x which can lead to a global switching for the pathway of reactive flux and thus the reduced mechanism itself must change. We have found that a generalization of the familiar energetic span theory (EST) can account for pathway switching and can reduce the number of QM calculations to a manageable number, often just two or four structures per value of x. In the basic EST scheme of Kozuch and Shaik⁴⁸ ⁴⁹ ⁵⁰ ⁵¹, the rate is expressed as an effective one-step process where the activation energy involves the highest transition state (HTS) and lowest intermediate (LINT) along a single catalytic cycle. The HTS is the bottleneck to the cycle while the LINT is the state of highest occupation probability. Those two dominating structures combine to yield the maximal free energy of activation via $\Delta G_a^{EST}(x) = G^{HTS}(x) - G^{LINT}(x)$ with the TOF given by

$$\nu(\mathbf{x}) = \frac{k_B T}{h} \cdot exp\left(-\frac{\Delta G_a^{EST}(\mathbf{x})}{k_B T}\right) \tag{4}$$

[When back-reaction from products plays a role there may be an additional correction to $\Delta G_a^{EST}(x)$ from the reaction energy.] The central issue is how to identify the (HTS,LINT) pair that controls the kinetics at each value of x. We have generalized the EST approach to more complex catalytic networks that involve multiple catalytic paths using an eigenvalue sensitivity analysis^{28 52 53} that is similar to Campbell's degree of reaction control.⁵⁴ The eigenvalues of the transition matrix are found to control the TOF and other kinetic properties of the network. A somewhat different spectral analysis was recently proposed by Peters.⁵⁵ In order to explore the method, for the 2D problem we shall actually compute the full chemistry network and locate the (HTS,LINT) pairs appropriate to each value of x. For the larger 3D problem, we use this information to simplify the network.

The eigenvalues and eigenvectors of T(x), $T(x)|v_j(x)\rangle = \lambda_j(x)|v_j(x)\rangle$ correspond to pure chemical-relaxation modes in the network and their rates. The TOF from eq. 3 is

$$\nu(x) = \frac{-1}{\sum_{k} \frac{C_k}{\lambda_k}} \tag{5}$$

where c_k are the projections of the normalized eigenvectors onto the initial state vector P_0 . Under most circumstances, the lowest absolute eigenvalue dominates the sum so $v(x) \approx |\lambda_1(x)|$ and $c_1 \approx 1$ and the eigenvector $|v_1(x)\rangle$ describes the occupation probabilities along the dominating chemical pathway. The exception is when the projection of the lowest eigenvector onto the AS is nearly zero and then the lowest two eigenvalues are generally necessary for the TOF. This

corresponds to an unproductive chemical path that is nearly uncoupled to the AS vector P_0 . The lowest absolute eigenvalue is well approximated by the EST expression, eq. (4). It is important to note that the higher eigenvalues also seem to be accurately approximated by a similar formula using other pairings of barrier and well energies. Thus, if we represent the activation energy for the jth eigenvalue as

$$\Delta G_{a,j}(\mathbf{x}) = G_j^{HTS}(\mathbf{x}) - G_j^{LINT}(\mathbf{x})$$
(6)

we have

$$\left|\lambda_{j}(x)\right| \approx \frac{k_{B}T}{h} \cdot exp\left(-\frac{\Delta G_{a,j}(x)}{k_{B}T}\right)$$
 (7)

To identify the correct (HTS,LINT) pairing for each eigenvalue we employ a sensitivity analysis where

Sensitivity Index of
$$\lambda_j = k_B T \cdot \frac{\partial ln(|\lambda_j(x)|)}{\partial G_i(x)}$$
 (8)

with the highest sensitivity structures yielding (HTS,LINT) pairs. Comparing eqs. (7) and (8), we note that a measure of the accuracy of the EST approximation is that the sensitivity index w.r.t. HST should be -1 and w.r.t. LINT should be +1. Further details of the method are provided in the SI.

D. Optimization Method

To maximize the TOF, we minimize the phenomenological free energy of activation $\delta G_a(\mathbf{x})$, where $\delta G_a(\mathbf{x}) \stackrel{\text{def}}{=} -k_B T \cdot ln\left(\frac{h}{k_B T}\nu(\mathbf{x})\right)$, as a function of the continuous disorder parameters \mathbf{x} subject to feasibility constraints that might restrict the range of \mathbf{x} . The quantity $\delta G_a(\mathbf{x})$ clearly minimizes at precisely the same place where $\nu(\mathbf{x})$ maximizes. Selectivity optimization is accomplished by maximizing the TOF projected unto the desired chemical pathway. The general nonlinear optimization problem can be written in standard notation as

$$x^* = argmin(f(x))$$
 (9)

$$g_1(x) \le 0$$

$$g_2(x) \le 0$$

:

$$h_1(x) = 0$$

 $h_2(x) = 0$
:

where f is the objective, the g's define inequality constraints and the h's define equality constraints. The optimization is carried out using the Scipy.optimize library in Python employing the nonlinear trust region constrained 'trust-constr' option. This algorithm is based on the primal-dual version of the method of Byrd et al.⁵⁶ This strategy is based on a barrier approach that employs sequential quadratic programming and trust regions to solve the sub-problems occurring in the iteration steps. To optimize the TOF, the objective function can be chosen to be either the exact $\delta G_a(x)$ from the full network or the EST approximation. For the latter, simpler, choice the objective is the non-differentiable function

$$f(\mathbf{x}) = \max_{\Delta G_{a,i}(\mathbf{x})} \left(\Delta G_{a,1}(\mathbf{x}), \Delta G_{a,2}(\mathbf{x}), \dots \Delta G_{a,i}(\mathbf{x}), \dots \right)$$
 (10)

where $\Delta G_{a,i}(x)$ are all the activation energies of the competing paths. Various convergent optimization techniques based on subgradient methods exists for non-differentiable functions although they tend to perform poorly. A superior choice is the smooth approximate

$$f(x) \to \bar{f}(x) = \frac{1}{\alpha} \cdot \ln\left(\frac{1}{e^{-\alpha\Delta G_{a,1}(x)}} + \frac{1}{e^{-\alpha\Delta G_{a,2}(x)}} + \cdots\right)$$
(11)

which is very close to the exact result $\delta G_a(x)$ for a single path reaction when we set $\alpha = k_B T$ and smoothly combines multiple pathway contributions. The most efficient optimization algorithms require approximate gradients and Hessians of the objective for Newton stepping. Since many QM methods provide such information as byproducts in determination of saddle points and wells, we shall assume they are available.

The choice of constraint functions in eq. (9) requires physical insight. We note that since $\delta G_a(x)$ represents a free energy difference between states with the same values of the disorder parameters, x, the internal strain energy of the silica support is cancelled out in the objective. This allows the algorithm to search out highly unstable and improbable support structures in either the pre-catalyst or the activated catalyst that may be highly reactive. However, we expect that highly unstable structures would be unlikely to form or would be very likely to decay from an AS. To exclude this unrealistic possibility, we constrain the values of x to lie in the feasible set defined within the overlap of the energy spheres of the lowest AS, i.e. $G_{AS}^0(x) \leq G_{MAX1}$ and the precatalyst $G_{pre-cat}^0(x) \leq G_{MAX2}$. Thus there are two inequality constraints,

$$G_{AS}^{0}(x) - G_{MAX1} \le 0$$

$$G_{pre-cat}^{0}(x) - G_{MAX2} \le 0$$
(12)

The numbers G_{MAX1} and G_{MAX2} are set after some experimentation and must lie above the highest chemically relevant barrier. The constraint functions are computed at the same level of QM as the chemical structures. In general, we observe the FS formed from the intersection of the two energy spheres forms a compact lens-shaped region in disorder space.

3. Results

A. Two-dimensional model

Focusing now in detail on the 2D model, the TOF obtained using full chemistry, v(x), obtained at T=323.15° K at fixed reagent concentration is depicted in Fig. 3a. This activity map shows a range of over ten orders of magnitude and clearly reveals zones of high activity which are sought in the maximization of v(x). The phenomenological free energy of activation, $\delta G_a(x)$ is also plotted as comparison. As a guide to the eye, the local maximum versus rvo is shown, i.e. $\max_{R_{VO}} v(r_{VO}, r_{OO}) = v_{max}(r_{OO})$ which follows the curved ridgeline that is superimposed on the contour; this ridge is equivalent to the minimum valley seen for $\delta G_a(x)$. This narrow ridge represents the region of highest activity for potential anchoring sites of the vanadium complex and is the target region for TOF optimization in a synthetic process. Indeed, the inset in Fig. 3a shows a one-dimensional cut at roo=3.25 Å that exhibits a typical volcano curve of TOF versus the single disorder parameter rvo. One can imagine the synthesis of a series of catalytic samples with distributions of disorder that follows such a one-dimensional path, represented heuristically in Fig. 3a by the series of dashed ovals superimposed on the disorder pathway. The present problem exhibits distinct multiple chemical pathways as shown in Fig. 2c. The selectivity of kinetic flux along those pathways can be extracted using the same sort of mathematics as the overall TOF, projecting the steady state flux onto the specific pathways, with the resulting selectivity map shown in Fig. 3b. Although kinetic flux along pathway 7 dominates in most regions, there are parameter regions of high preference for path 5. This path-switching behavior is familiar from the study of product selectivity where two competing reaction paths are controlled by the relative energy of two transition states that lead to different products through a common intermediate.^{28 57 58}

Optimization of a catalyst for selectivity at an atomic level involves the tuning of relative activation energies controlling different paths in the design space.⁵⁹

It is clear that the TOF and selectivity maps exhibit multiple stationary points and thus they are not simple convex functions of the design variables. However, the numerical methods developed around convex optimization have proven quite robust in complex applications when sufficient precautions are taken to constrain the domain. For the present problem, this involves setting G_{MAX1} and G_{MAX2} so that a single well-defined minimum exists. The lens-shaped FS shown in Fig. 3c is found to exhibit a single minimum for which the optimization algorithm performs well.

To illustrate the efficiency of this scheme, we consider optimizing the activity at 323.15° K using the full chemistry model and the optimization method of Byrd et al.56 As seen in Fig. 4, the optimization occurs quickly and the optimum disordered state is discovered with high accuracy after less than 10 steps. The initial guess is arbitrary, and any choice leads to the same optimum. If the optimization is carried out using the full chemistry, each step requires a complete evaluation of the free energies of the chemical network. The optimization package also requires approximate gradients and Hessians of the objective function $\delta G_a(x)$ and the constraint functions at each structure which are available for B3LYP. We also note that the method does not require a feasible start, so the random initial guess for x need not obey the constraints. A general observation in optimization theory is that an efficient higher-order algorithm will converge within 50 or fewer steps even in high-dimension or with complicated (but approximately convex) functions. This is a tractable number of quantum chemistry calculations provided that the chemical network does not grow too large. In the present case, convergence to within chemical accuracy occurs after only a handful of Newton steps. A schematic illustration of the optimization problem is given in Fig. 5 showing the relation of the TOF to the free energy and application to two and four state models. For a two state model \mathbf{x}^* occurs at the at $\min_{\mathbf{x}} [\Delta G_a^{EST}(\mathbf{x})]$. For four states (and any higher number), \mathbf{x}^* occurs at $\min_{\mathbf{x}} \left[\max_{\Delta G_{a,i}(\mathbf{x})} (\Delta G_{a,1}(\mathbf{x}), \Delta G_{a,2}(\mathbf{x}), \dots \Delta G_{a,i}(\mathbf{x}), \dots) \right]$ at which point the objective can be non-differentiable.

We now consider how mechanism reduction might work for the 2D model. In Figs. 6a and 6b we plot numerically determined HTS and LINT which are color-coded and labeled by structure

number. We see the identity of the (HTS,LINT) varies profoundly as a function of x and the plot is characterized by numerous boundary curves where barrier or well energies are equal. In Fig. 6c we use these identifications to compute the free energy, $\Delta G_a^{EST}(x)$. We see the agreement between the generalized EST result and the kinetically exact quantity, $\delta G_a(x)$, Fig. 6d, is impressive and the only visible difference is a subtle smoothing of the exact $\delta G_a(x)$ around the transition boundaries between (HTS, LINT) pairings. It is interesting to note that the optimum disorder, x^* , lies on the boundary between two (HTS, LINT) pairs, specifically between the structures (25, 24) and (23, AS). Furthermore, the constrained optimum $v_{max}(R_{00})$ lies along this boundary line. Thus the physical meaning of x^* is the point that the activation energy for the first H-atom addition to styrene is exactly equal to the activation energy for the addition of the second H-atom. In terms of optimization theory, we conclude that the mechanism reduction method should include four states in the generalized theory rather than just the two states of the basic EST. If optimization paths pass between three distinct zones of (HTS,LINT) pairing, then potentially six states would be required, and so forth.

In Fig. 7 the eigenvalue sensitivity analysis and generalized EST theory is illustrated. In Fig. 7a, several low-lying eigenvalues of the transition matrix are plotted versus the disorder parameter r_{VO} holding r_{OO} fixed. Numerous avoided crossings are observed at which points the definition of (HTS,LINT) are abruptly changing. Also plotted are the EST approximations to these eigenvalues which show a good agreement. In Figs. 7b and 7c the eigenvalue sensitivity indices of the lowest two eigenvalues are shown immediately before and after the avoided crossing of those eigenvalues. The identification of (HTS,LINT) pair is seen to jump from (25,24) to (23,AS) at the avoided crossing. We note that the exact \mathbf{x}^* obtained from the Byrd *et al.*⁵⁶ method using the full chemistry model is found to occur nearly exactly along this eigenvalue crossing seam.

B. Three-dimensional model

Using the EST model with the four states (25, 24) and (23, AS) that we identified as most important, we have also tested the optimization strategy for the 3D representation with disorder coordinates (r_1, r_2, r_3) . The optimization path and energy surfaces are plotted in Fig. 8. Since it is difficult to visualize the free energy surfaces in a three-dimensional disorder space, we have plotted the free energy along the intersection surface where the free energy barriers are equal, i.e., $\Delta G_{a,1}^{EST}(\mathbf{x}) = \Delta G_{a,2}^{EST}(\mathbf{x})$. It is seen that the algorithm quickly optimizes to a geometry that is

independent of the initial conditions. The efficiency of convergence depends somewhat on starting point but typically we achieve convergence to within <1% within about a dozen Newton steps. As indicated in the figure, the optimal point is found to lie on the intersection surface of $\Delta G_{a,1}^{EST}(\mathbf{x})$ and $\Delta G_{a,2}^{EST}(\mathbf{x})$ although the arbitrary initial condition lies well off this surface.

The molecular geometries of the optimally engineered disordered state of the 3D system are roughly consistent with the result obtained in the 2D representation. However, there are some detailed differences in the configurations since the two systems are constrained differently. We note that 3D representation considers only variation of the silica configuration while the 2D representation considers variation of one silica coordinate and one coordinate for bonding the vanadium to the support.

C. Higher dimensions

The success of the optimization strategy for the present case suggests the following computationally efficient procedure that can be applied to a very high-dimensional representation of the active site heterogeneity. First, the full mechanism is computed at a few representative values of the disorder parameters, which are used as a screening to identify a small set of potential (HTS, LINT) pairs. Then a much smaller set of structures is used to minimize the activation energy obtained from QM versus x. This has the great advantage that QM for the full array of barriers and wells does not need to be computed for each step. Naturally, it is possible that the search may wander into a region of x where the (HTS, LINT) structures involve new pairs. Hence, at a later stage of the calculation it is wise to compute the full network at the near optimized x^* to verify the correct structures have been included. If not, the process can be repeated with new choices. In the present case, the pairs (25, 24) and (23, AS) are all that is required to optimize the TOF to high accuracy in 3D. If the microkinetic mechanism is not too large, it may also be computationally feasible to directly optimize the full chemistry model. This more QM intensive approach has the advantage that the pathway-switching effect is automatically included in the TOF without the need to perform a sensitivity analysis.

D. Scaling Relations

The optimality of equal activation energies is highly reminiscent of the Sabatier principle that has been successfully invoked previously 60 to explain volcano plots as a function of an intermediate energy for a variety of heterogeneous catalytic systems. This principle states that the

best catalyst is obtained when an intermediate is bound at the best compromise value between the attachment step and the release step of the cycle. It has been shown that using an intermediate binding energy as an independent variable, one finds approximate Evans-Polanyi-Brønsted type linear scaling relations for transition states for diverse systems such as ammonia synthesis, ethanol conversion, and electrochemical reduction. 61 62 63 Does disorder fit into this pattern? As a test, we computed the energies of all the wells and barriers versus a key intermediate energy, viz. that for structure 24 where styrene has been partially hydrogenated. These results show a good linear relation and are presented fully in Fig. 9. The individual dots represent geometries sampled over the full range disorder parameters computed by QM. In-Fig. 10 we show three activation energies versus G_{24} : $\Delta G_{a,1} = G_{25} - G_{24}$ (path 7), $\Delta G_{a,2} = G_{23} - G_{AS}$ (path 7), and $\Delta G_{a,3} = G_{20} - G_{AS}$ (path 5). The scatterplot of points represents the full (r_{vo}, r_{oo}) 2D-disorder plane and it is seen that an approximate linear relationship does indeed develop. It is seen that the crossing of the two activation energies, $\Delta G_{a,1}$ and $\Delta G_{a,2}$, occurs precisely at the previously obtained crossing seam obtained from the avoided crossing of the eigenvalue surfaces $\lambda_1(x) \approx \lambda_2(x)$ plotted in Fig. 5c. Interestingly, the activation energy on path 5, $\Delta G_{a,3}$, also shows a linear scaling with G_{24} although path 5 does not include state 24.

The success of the linear scaling relationship implies that the most important structures in the chemical reaction network are all approximately functions of a single independent variable, $G_{24}^0(x)$. This simplifies the chemical network and collapses the disorder space both into one independent variable. A search procedure for optimality is then $\underset{G_{24}}{\operatorname{argmin}} \left(\Delta G_{a,1} - \Delta G_{a,2} \right)^2$ where the disorder parameters are set by the requirement that two key activation energies are equal. Naturally, the question arises whether additional independent variables might be required for more complicated chemistry or higher dimensional models of disorder or when multiple binding sites contribute. This might be described as circumventing or breaking linear scaling. In the present application, the "width" of the scatterplots around the straight line represents the influence of additional secondary degrees of freedom that correspond to different locations along the crossing seam that possess modestly differing TOF's. The uncertainty in the crossing point, $\Delta G_{\text{non-linear}}$ in Fig. 9, reflects the variation in TOF along the crossing seam. We leave it as an open empirical question how these additional degrees of freedom can be added in ranked influence.

4. Conclusion

Active site heterogeneity in a catalytic sample can originate in multiple ways but will invariably lead to a distribution of catalytic performance and provides a new opportunity to improve catalytic design. Activity hot spots in a sample can be enhanced by a rationally guided synthesis based on a local representation of the disorder. The question explored here is how these hotspots may be located using ab initio QM which then provides targets for a synthetic strategy. Practical control parameters can include variables such as dopant concentration, nanoparticle size, nanoparticle composition, substrate porosity, or annealing rates. The approach we have suggested involves several steps. First, a mechanism is parameterized using a small number of local disorder coordinates that are suspected to strongly influence the TOF or selectivity. The kinetics of this initial parameterization is then used to select a number of key structures that control the performance of the catalyst, here that number was four, i.e., two TS and two INT. Then, employing a nonlinear optimization method, the optimal values of the disorder coordinates are computed from the QM energetics of the reduced mechanism. The low-dimensional disorder space is then expanded to include more of the local environment and, thereby, a more accurate optimum is found. Here, we stopped at three dimensions but can be made much higher. Since the efficient nonlinear optimization relies on Newton stepping, the QM calculations should provide approximate gradients and Hessians for the optimized geometries of the key TS and INT structures.

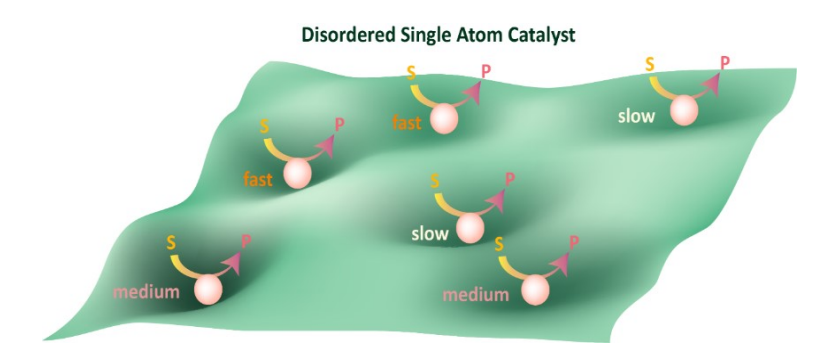
The main complexity of optimizing the active site environment is that reaction path can change as a function of the disorder coordinates. This implies that different locations on the sample can proceed through different controlling mechanisms. We have found that the optimal environment often occurs along the boundary surfaces between such reaction paths in direct analogy to the Sabatier principle. Direct optimization in a high-dimensional disorder space remains feasible even in such cases using the eigenvalue methodology induced here.

Acknowledgements

This work was supported by the National Science Foundation through grant CHE1664555. This work was also supported by the U.S. Department of Energy (DOE) Office of Basic Energy Sciences, Division of Chemical Sciences, Geosciences, and Biosciences, Catalysis Science

Program under Contract DE-AC02-06CH11357 (Argonne National Laboratory). All DFT calculations were performed using the computational resources provided by the Laboratory Computing Resource Center (LCRC) at Argonne National Laboratory (ANL) and the Texas Advanced Computing Center (TACC) at the University of Texas at Austin.

Supporting Information: The Supporting Information is available free of charge at https://pubs.acs.org/doi/10.1021/acs.jpcc.0c01304. The results of the quantum calculations for the properties of the transition states and intermediates of the kinetic network as functions of the disorder coordinates. A detailed description of the eigenvalue sensitivity method and the Arrhenius extrapolation method needed to stabilize that transition matrix (PDF).



TOC Graphic

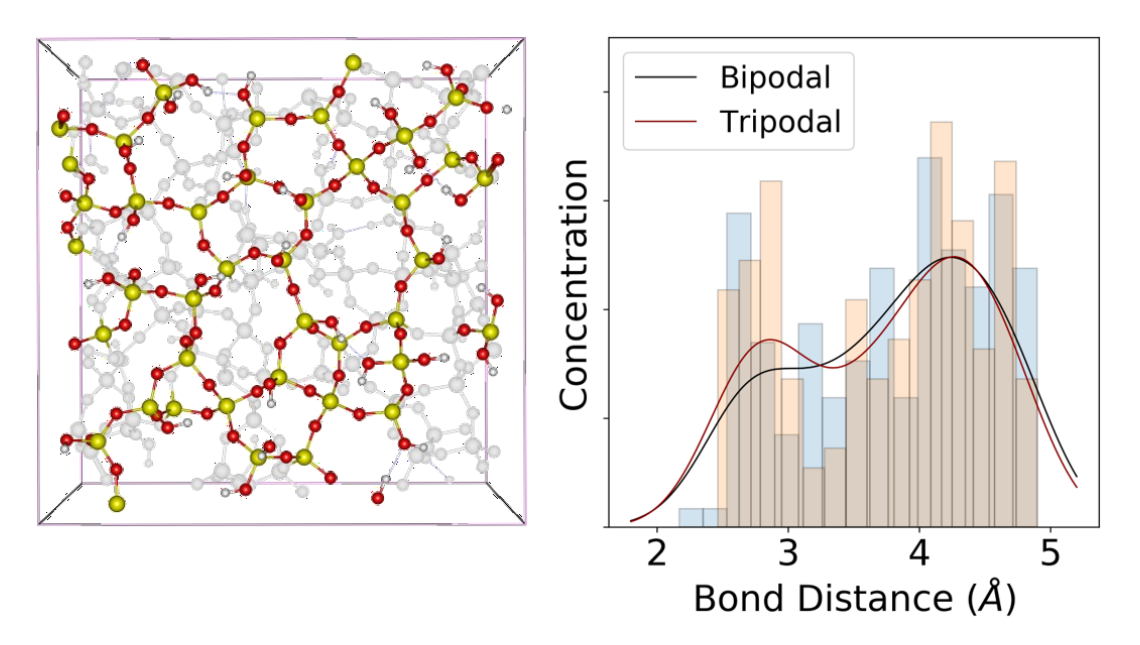


Fig. 1. A representative computational structure of amorphous silica, obtained following the methods of refs.32 and 33 (left), along with the distribution of O-O bond distances for all potential binding sites (right). The model shows the top monolayer layer of amorphous silica (Si – yellow, O – red, H – white) while the bulk is grey. The kernel density estimation distributions are based along with a histogram of calculated O-O bond distances surrounding potential binding sites. Bipodal and tripodal grafting sites are represented via the blue and orange bars, respectively, as well as the black and red curves, respectively.

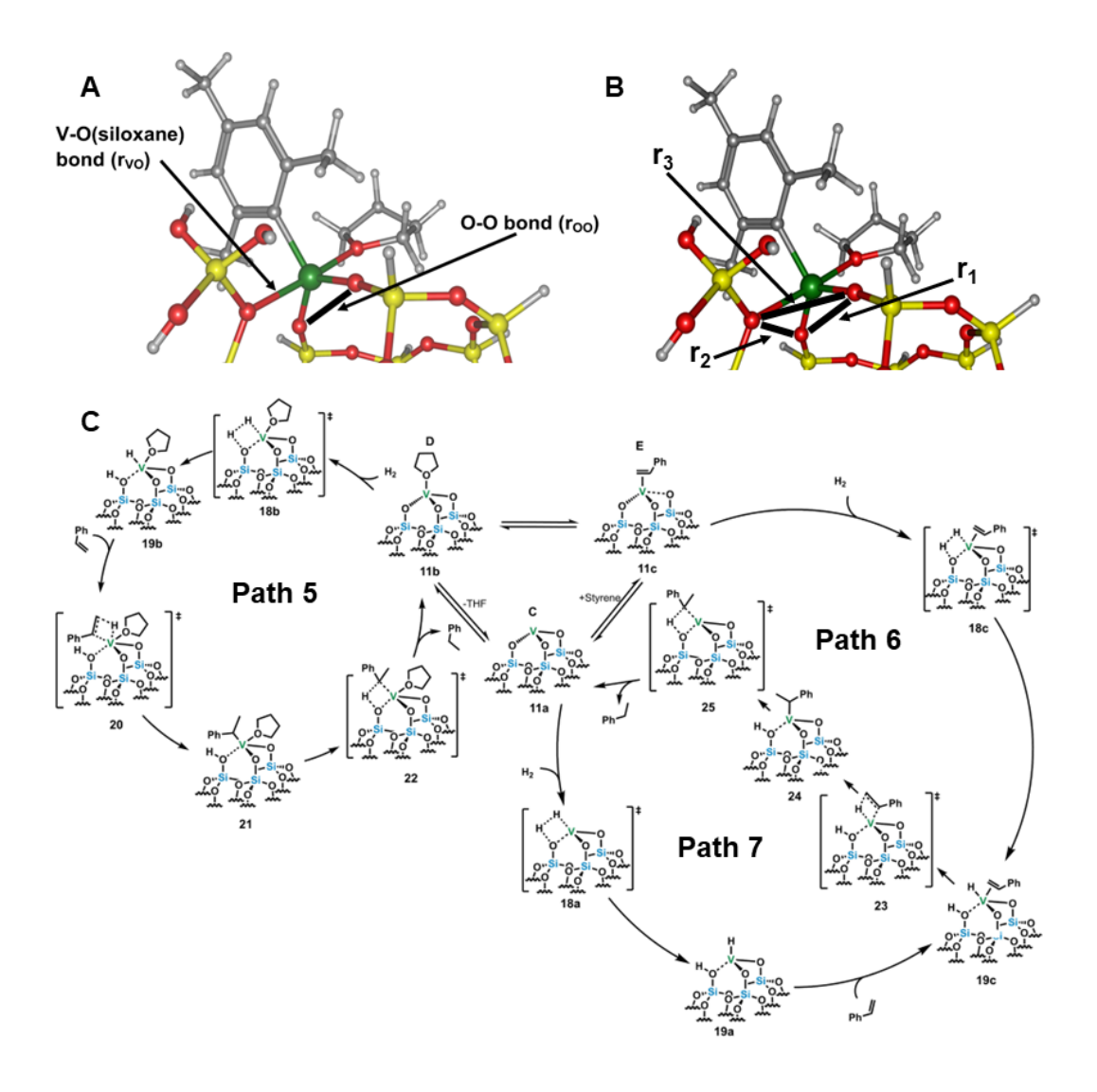


Fig. 2. The structure and kinetics of the silica supported organovanadium catalyst. In (a), the atomic level cluster model of the proposed pre-catalyst grafted to the silica support at a tripodal trigonal bipyramid site with a silanol donor, $(\equiv SiO)_2V(Mes)(THF)$. The structure was obtained at the B3LYP/CEP-31G level of theory. The atoms are coded as V=Green, Si=Yellow, O=Red, C=Gray, H=White. The two local coordinates r_{vo} and r_{oo} are indicated in the figure. In (b), the coordinates r_1 , r_2 , and r_3 of the 3D model are shown. In (c), the microkinetic model for the overall process styrene+H₂ \rightarrow ethyl benzene is shown. The active sites (AS) labeled D, C, and E are created by the activation process and are defined as the species after irreversible product release. The three cycles 5, 6, and 7 are kinetically coupled. The active sites are found to rapidly interconvert on the timescale set by the TOF.

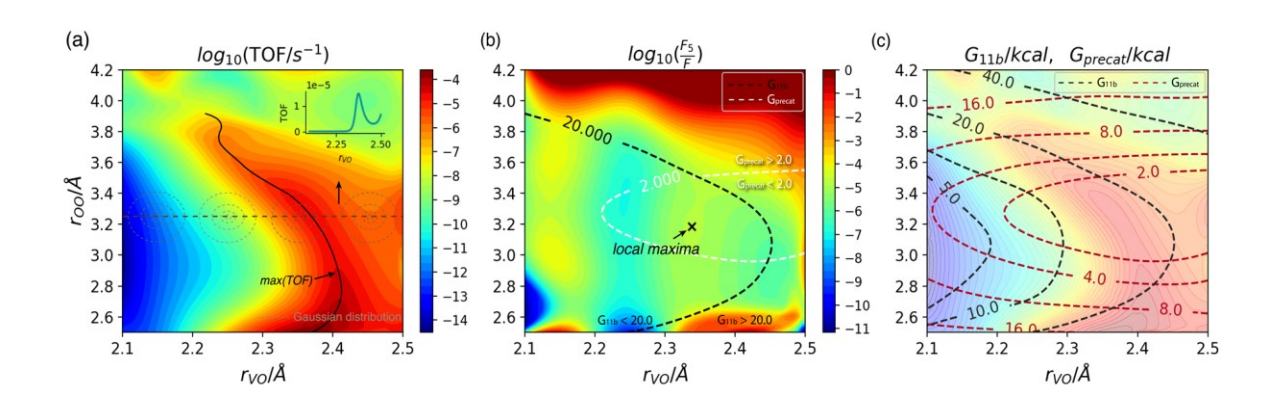


Fig. 3. Activity and selectivity maps in a two-dimensional disorder space. In (a), zones of high activity are show in red and low activity in blue on a logarithmic scale. The conditions chosen are T=323.15°K, [Styrene]=1M, [H₂]=5M, and [THF]=0.01M. The superimposed solid line shows the ridge of constrained maxima, $v_{max}(R_{00})$. Along the cut at roo=3.25 Å the TOF exhibits a volcano curve shown in the inset. The oval shaped distributions overlaying the cut heuristically represent a sequence of synthetic samples displaying the volcano plot. In (b), the selectivity of the reactive flux following pathway 5 is shown where red denotes high flux. In regions of high overall activity, the flux is dominated by pathway 7 although there is a small local maximum of pathway 5 flux indicated by the cross. The dashed lines bound the feasible set with the choices values $G_{MAX1} = 2 kcal/mol$ and $G_{MAX2} = 20 kcal/mol$. In (c) the feasible set of permitted disorder values is the lens shaped region. The contour lines the level sets for the functions $G_{AS}^0(x)$ and $G_{pre-cat}^0(x)$.

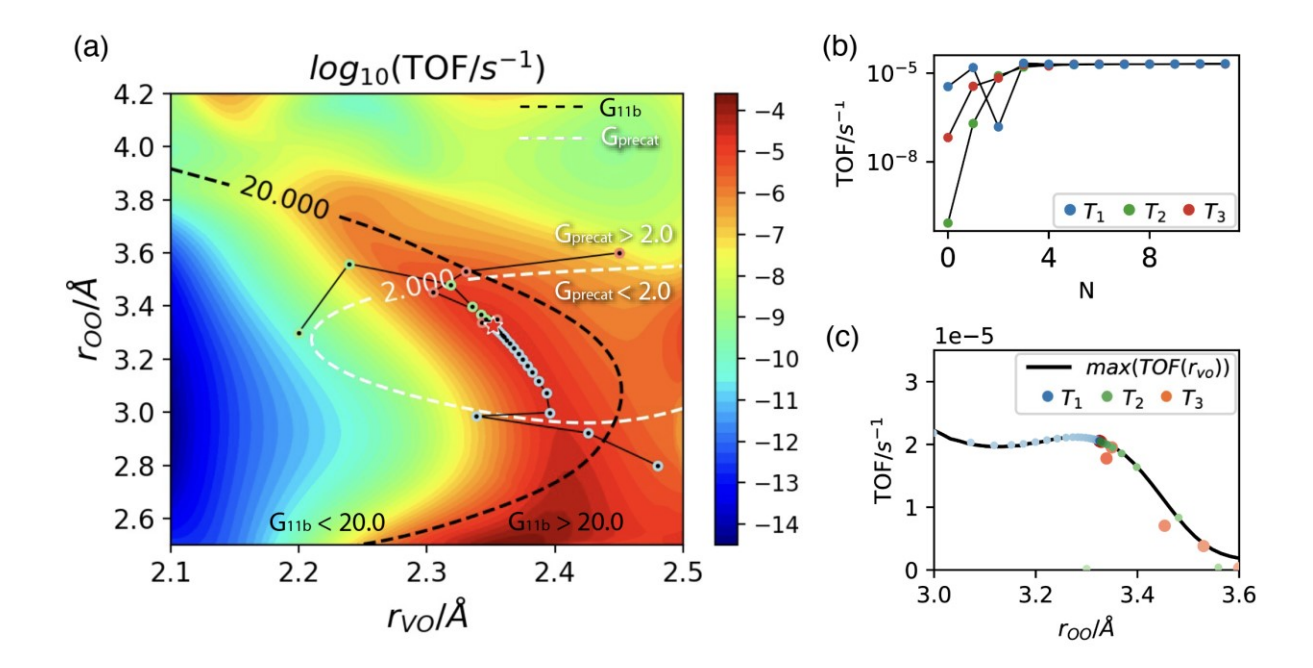


Fig. 4. Three optimization pathways, T_1 - T_3 , which maximize the TOF in a two-dimensional representation of disorder with full chemistry. Three initial conditions outside the FS were randomly selected and converge to the same optimal point. In (a), the optimization paths are shown superimposed on the TOF objective function and boundaries to the FS are depicted with dashed lines. In (b), the convergence of the objective function (the TOF) is shown as a function of the algorithmic step N. In (c), the optimization paths are plotted in (TOF, r_{oo}) space along with the position of the ridge $v_{max}(r_{oo})$. Within a few steps, the trajectories converge to the ridge and thereafter approaches the maximum more slowly.

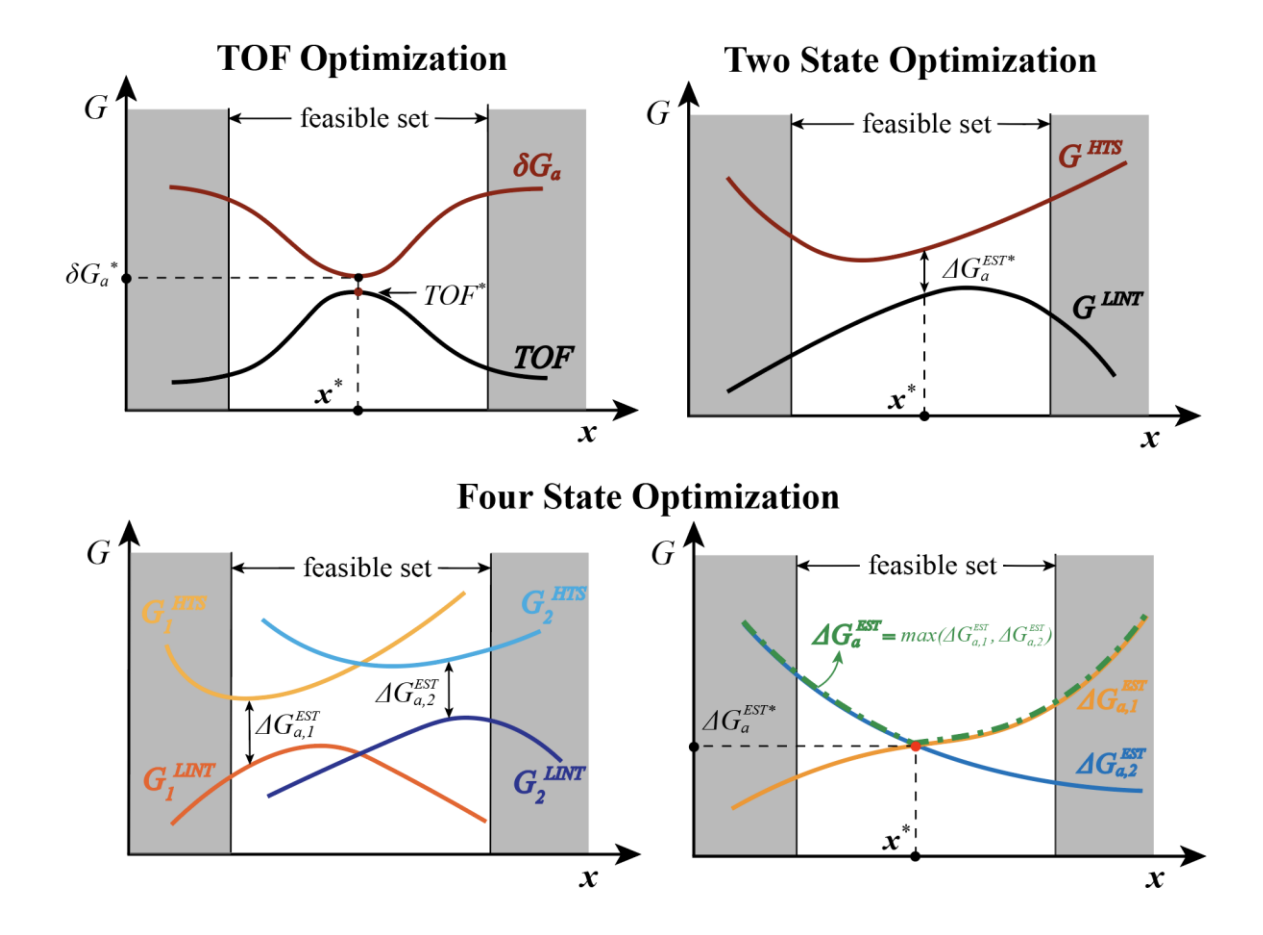


Fig. 5. A schematic diagram showing various optimization strategies. In the first panel, the full TOF is optimization versus disorder coordinate x. The maximizer of the TOF, x^* , is same as the minimizer of phenomenological free energy of activation. In the second panel, a two state optimization involves minimizing the difference between the barrier energy, G^{HTS} , and the well energy G^{LINT} . In the lower panels the four state optimization is represented. Two activation energies $\Delta G_{a,1}^{HTS}(x)$ and $\Delta G_{a,1}^{HTS}(x)$, are found from the difference between two (HTS,LINT) pairs. The greater of $\Delta G_{a,1}^{HTS}(x)$ and $\Delta G_{a,1}^{HTS}(x)$ at each x defines the overall free energy of activation $\Delta G_a^{EST}(x)$ of the EST. The minimum of $\Delta G_a^{EST}(x)$ defines the optimum, x^* .

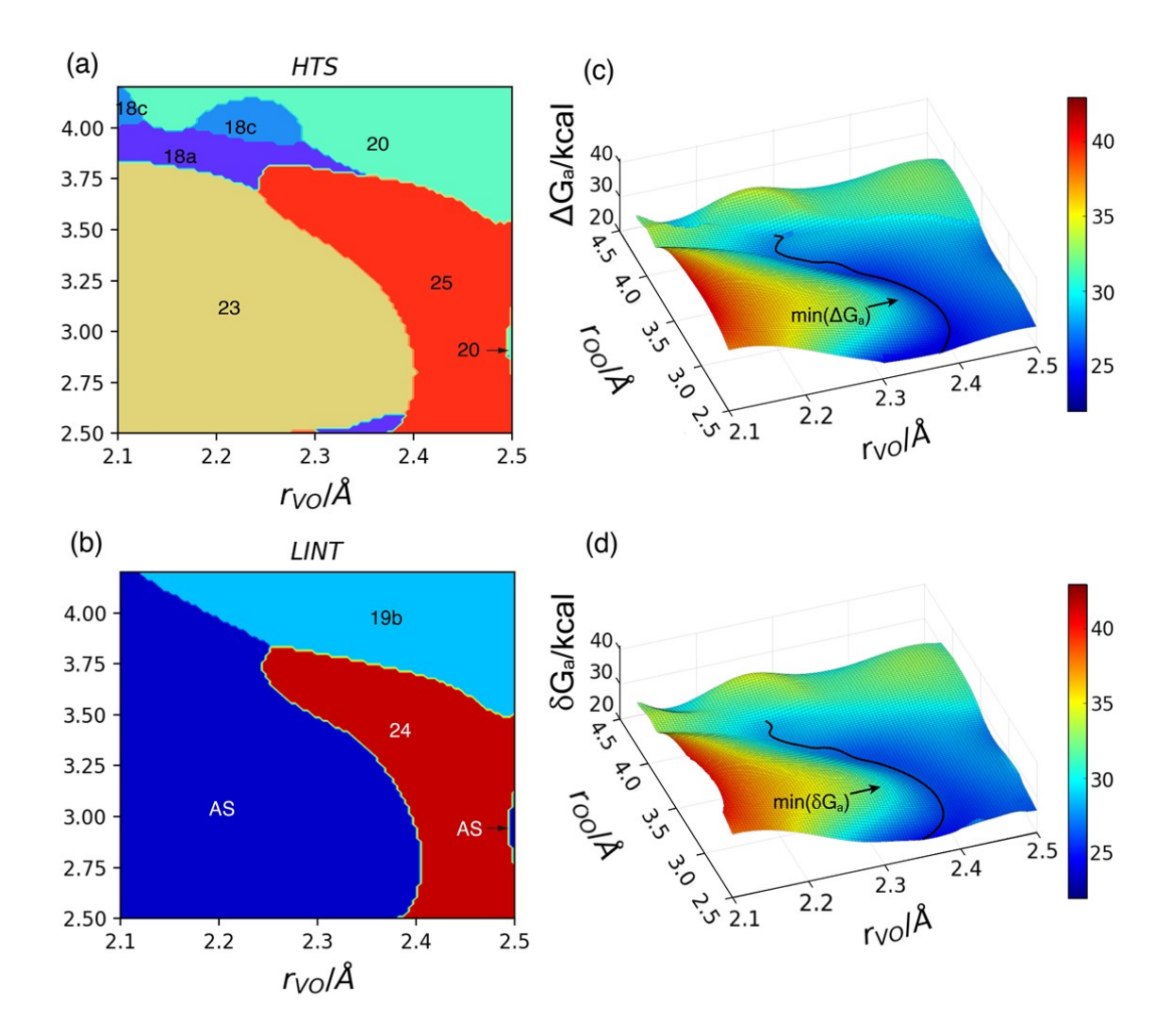


Fig. 6. The generalized energetic span theory in two-dimensions. In (a) and (b) the HTS and LINT are shown as functions of the disorder coordinates. These designations are determined using a sensitivity analysis of the TOF. The boundary lines between regions occur when the barriers and wells controlling the reactive flux undergo transition. In (c) the EST prediction of the effective activation free energy is shown versus x. In (d) the kinetically exact phenomenological free energy is shown which agrees very well with the EST approximation. Note that the $\min(\delta G_a(\mathbf{x}))$ lies extremely close to the eigenvalue avoided crossing curve $\lambda_1(\mathbf{x}) \approx \lambda_2(\mathbf{x})$ and their plots are indistinguishable.

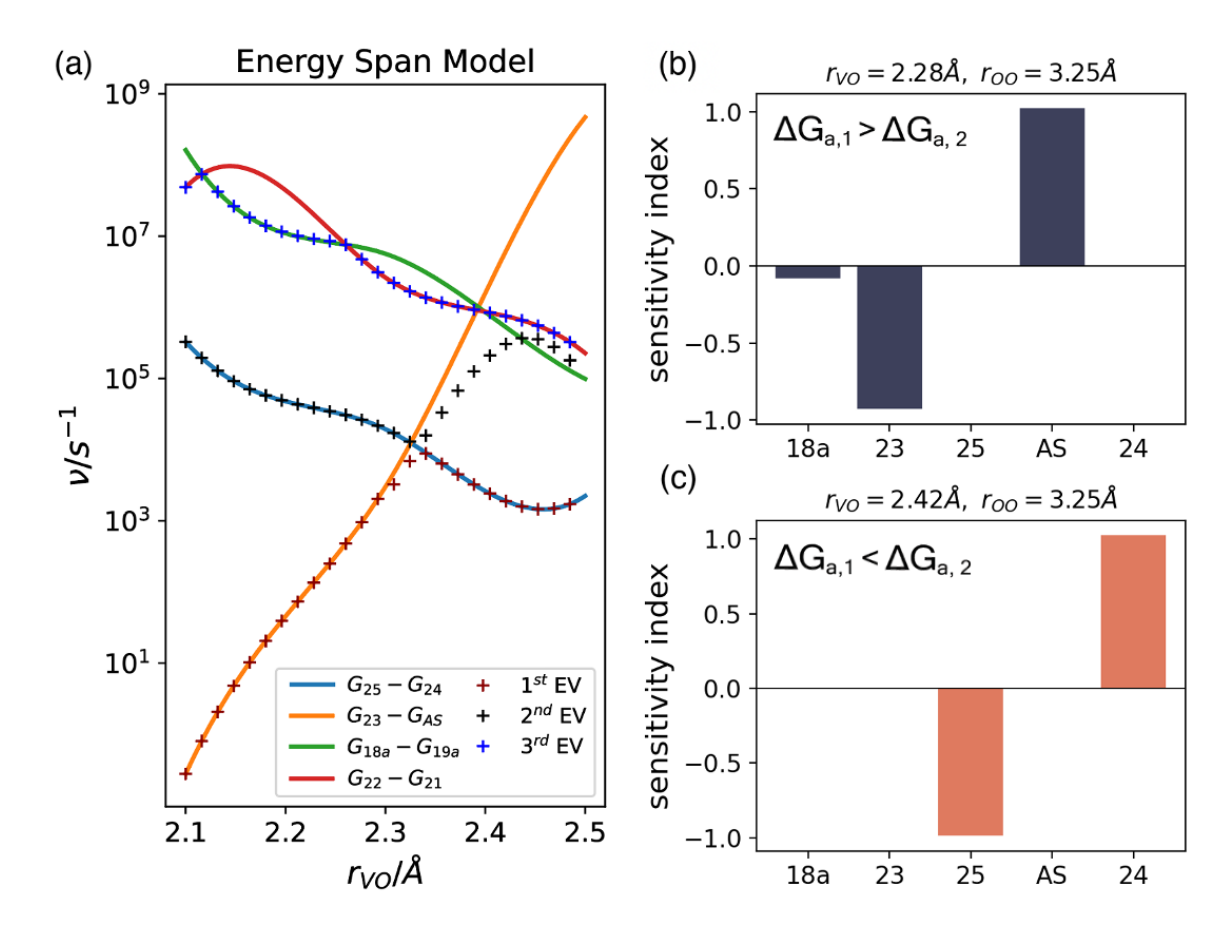


Fig. 7. Eigenvalues of the transition matrix as a function of the disorder parameter r_{VO} holding the value of r_{OO} fixed at 3.25Å compared with the sensitivity spectrum. The concentrations of the reagents were chosen to be [ST]=1M, [H₂]=5M, and [THF]=0.01M. In (a), the lowest three eigenvalues computed from the full T-matrix are shown along with predictions of EST. There is a sharp avoided crossing of the lowest two eigenvalues at r_{VO} =2.32Å at which point the TOF maximizes. In (b) the sensitivity index of the lowest eigenvalue reveals the appropriate choices for the pairing (HTS,LINT). The upper panel shows the spectrum at a value of r_{VO} slightly below the crossing point and lower panel shows the spectrum slightly above the crossing point. The result clearly shows that (HTS,LINT) goes from (AS,23) to (24,25) abruptly at the crossing point.

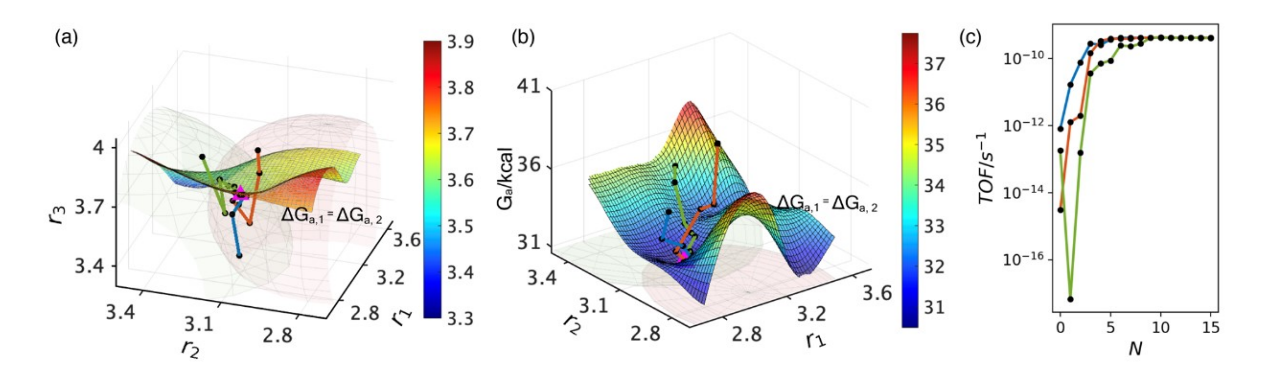


Fig. 8. Several optimization trajectories for the three-dimensional disorder model. The three random trajectories are shown which are started from random unfeasible initial conditions. (a) The trajectories are shown (r_1, r_2, r_3) -space along with three surfaces: the crossing surface for the two activation free energies, $\Delta G_a^1(r_1, r_2, r_3) = \Delta G_a^2(r_1, r_2, r_3)$, multicolored; the boundary surface of the constraint on the precatalyst, $R_{PC} > ||x - x_0^{PC}||$, in red; and the boundary surface of constraint on the AS, $R_{AS} > ||x - x_0^{AS}||$, in green. In (b) the same trajectories are plotted in $(r_1, r_2, Energy)$ space along with the crossing surface for activation energies. In (c) the convergence of the TOF is shown as a function of optimization step. Most trajectories quickly approach the crossing surface and then more slowly approach the overall optimum.

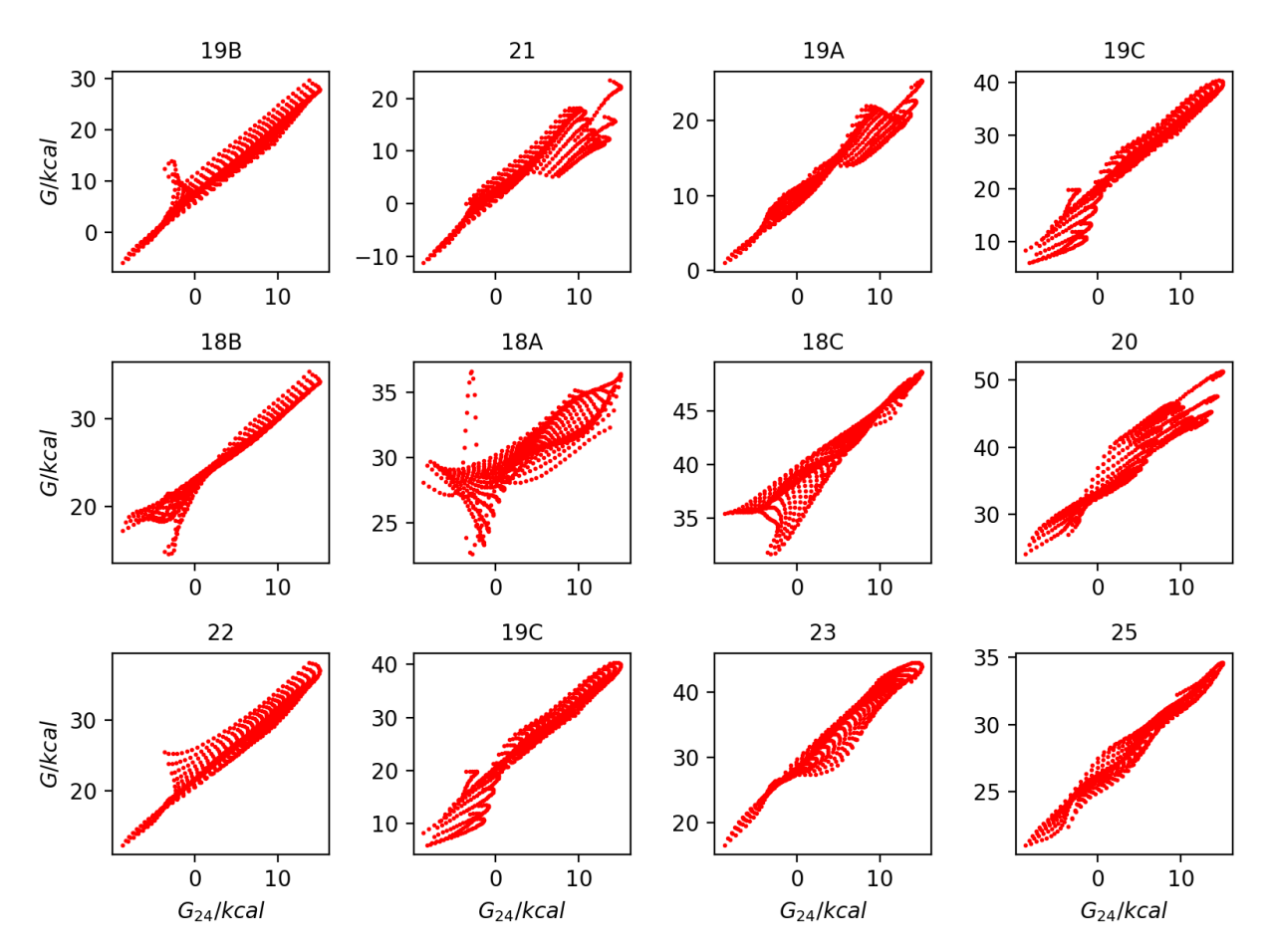


Fig. 9. Linear scaling relations for the barrier and well free energies as a function of the intermediate free energy, G_{24} in the two-dimensional disorder model. The points represent a grid values, (r_{VO} , r_{OO}), that span the full range of disorder space given by Table S1.The temperature is chosen to be 323.15 K and the free energies reflect the reagent concentrations, [THF]=0.01M, [Styrene]=1M, and [H₂]=5M. The largest outliers to linear scaling occur at the edge of the grid.

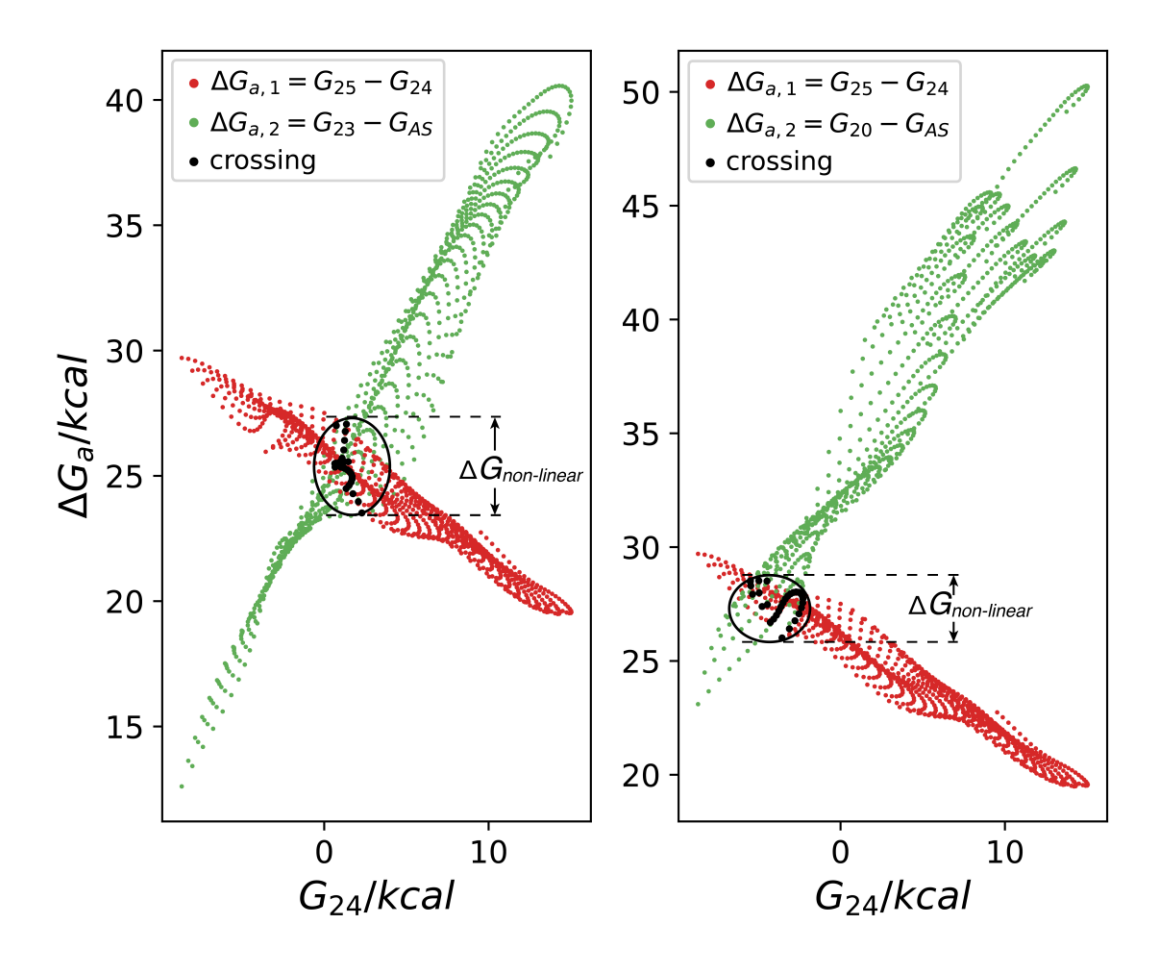


Fig. 10. Linear scaling of three activation free energies as a function of the binding free energy of the intermediate, **24**. The zero for G_{24} is taken as the lowest active site. In (a) the activation energy $\Delta G_{a,1} = G_{25} - G_{24}$ is plotted in red and $\Delta G_{a,2} = G_{23} - G_{AS}$ is plotted in green. The scatter of points represents a uniform array of x-values with $r_{00} < 3.6$ Å. In (b), the $\Delta G_{a,1} = G_{25} - G_{24}$ is again in red and $\Delta G_{a,3} = G_{20} - G_{AS}$ is in green. The black dots lie along the boundary line where the activation free energies are equal.

References

_

¹ Nørskov, J. K.; Bligaard, T.; Rossmeisl, J.; Christensen, C. H. Towards the Computational Design of Solid Catalysts. *Nat. Chem.* **2009**, *1* (1), 37–46.

² Schlexer Lamoureux, P.; Winther, K. T.; Garrido Torres, J. A.; Streibel, V.; Zhao, M.; Bajdich, M.; Abild-Pedersen, F.; Bligaard, T. Machine Learning for Computational Heterogeneous Catalysis. *ChemCatChem* **2019**, *11* (16), 3581–3601.

³ Foscato, M.; Jensen, V. R. Automated in Silico Design of Homogeneous Catalysts. *ACS Catal.* **2020**, *10* (3), 2354–2377.

⁴ Linic, S.; Jankowiak, J.; Barteau, M. A. Selectivity Driven Design of Bimetallic Ethylene Epoxidation Catalysts from First Principles. *J. Catal.* **2004**, *224* (2), 489–493.

⁵ Tsai, C.; Chan, K.; K. Nørskov, J.; Abild-Pedersen, F. Rational Design of MoS 2 Catalysts: Tuning the Structure and Activity via Transition Metal Doping. *Catal. Sci. Technol.* **2015**, *5* (1), 246–253.

⁶ Li, H.; Guo, S.; Shin, K.; Wong, M. S.; Henkelman, G. Design of a Pd–Au Nitrite Reduction Catalyst by Identifying and Optimizing Active Ensembles. *ACS Catal.* **2019**, *9* (9), 7957–7966.

⁷ Bligaard, T.; Nørskov, J. K.; Dahl, S.; Matthiesen, J.; Christensen, C. H.; Sehested, J. The Brønsted–Evans–Polanyi Relation and the Volcano Curve in Heterogeneous Catalysis. *J. Catal.* **2004**, *224* (1), 206–217.

⁸ Cheng, J.; Hu, P. Utilization of the Three-Dimensional Volcano Surface To Understand the Chemistry of Multiphase Systems in Heterogeneous Catalysis. *J. Am. Chem. Soc.* **2008**, *130* (33), 10868–10869.

⁹ Seh, Z. W.; Kibsgaard, J.; Dickens, C. F.; Chorkendorff, I.; Nørskov, J. K.; Jaramillo, T. F. Combining Theory and Experiment in Electrocatalysis: Insights into Materials Design. *Science* **2017**, *355* (6321), eaad4998.

¹⁰ Liu, X.; Xiao, J.; Peng, H.; Hong, X.; Chan, K.; Nørskov, J. K. Understanding Trends in Electrochemical Carbon Dioxide Reduction Rates. *Nat. Commun.* **2017**, *8* (1), 15438.

¹¹ Schlexer Lamoureux, P.; Winther, K. T.; Garrido Torres, J. A.; Streibel, V.; Zhao, M.; Bajdich, M.; Abild-Pedersen, F.; Bligaard, T. Machine Learning for Computational Heterogeneous Catalysis. *ChemCatChem* **2019**, *11* (16), 3581–3601.

¹² Esterhuizen, J. A.; Goldsmith, B. R.; Linic, S. Interpretable Machine Learning for Knowledge Generation in Heterogeneous Catalysis. *Nat. Catal.* **2022**, *5* (3), 175–184.

¹³ Ulissi, Z. W.; Medford, A. J.; Bligaard, T.; Nørskov, J. K. To Address Surface Reaction Network Complexity Using Scaling Relations Machine Learning and DFT Calculations. *Nat. Commun.* **2017**, *8* (1), 14621.

¹⁴ Goldsmith, B. R.; Sanderson, E. D.; Bean, D.; and Peters, B. Isolated catalyst sites on amorphous supports: A systematic algorithm for understanding heterogeneities in structure and reactivity. J. Chem. Phys, **2013**, 138(20), 204105.

¹⁵ Therrien, A. J.; Hensley, A. J. R.; Marcinkowski, M. D.; Zhang, R.; Lucci, F. R.; Coughlin, B.; Schilling, A. C.; McEwen, J.-S.; Sykes, E. C. H. An Atomic-Scale View of Single-Site Pt Catalysis for Low-Temperature CO Oxidation. *Nat. Catal.* **2018**, *I* (3), 192–198.

¹⁶ Nie, L.; Mei, D.; Xiong, H.; Peng, B.; Ren, Z.; Hernandez, X. I. P.; DeLaRiva, A.; Wang, M.; Engelhard, M. H.; Kovarik, L.; *et al.* Activation of Surface Lattice Oxygen in Single-Atom Pt/CeO2 for Low-Temperature CO Oxidation. *Science* **2017**, *358* (6369), 1419–1423.

¹⁷ English, B. P.; Min, W.; van Oijen, A. M.; Lee, K. T.; Luo, G.; Sun, H.; Cherayil, B. J.; Kou, S. C.; Xie, X. S. Ever-Fluctuating Single Enzyme Molecules: Michaelis-Menten Equation Revisited. *Nat. Chem. Biol.* **2006**, *2* (2), 87–94.

¹⁸ Xu, W.; Kong, J. S.; Yeh, Y.-T. E.; Chen, P. Single-Molecule Nanocatalysis Reveals Heterogeneous Reaction Pathways and Catalytic Dynamics. *Nat. Mater.* **2008**, *7* (12), 992–996.

¹⁹ Buurmans, I. L. C.; Weckhuysen, B. M. Heterogeneities of Individual Catalyst Particles in Space and Time as Monitored by Spectroscopy. *Nat. Chem.* **2012**, *4* (11), 873–886.

²⁰ Moffitt, J. R.; Bustamante, C. Extracting Signal from Noise: Kinetic Mechanisms from a Michaelis–Menten-like Expression for Enzymatic Fluctuations. *FEBS J.* **2014**, *281* (2), 498–517.

²¹ Zwanzig, R. Rate Processes with Dynamical Disorder. Acc. Chem. Res. 1990, 23 (5), 148–152.

²² Zhang, Z.; Zandkarimi, B.; Alexandrova, A. N. Ensembles of Metastable States Govern Heterogeneous Catalysis on Dynamic Interfaces. *Acc. Chem. Res.* **2020**, *53* (2), 447–458.

²³ Andoy, N. M.; Zhou, X.; Choudhary, E.; Shen, H.; Liu, G.; Chen, P. Single-Molecule Catalysis Mapping Quantifies Site-Specific Activity and Uncovers Radial Activity Gradient on Single 2D Nanocrystals. *J. Am. Chem. Soc.* **2013**, *135* (5), 1845–1852.

- ²⁴ Boyd, S.; Boyd, S. P.; Vandenberghe, L. Convex Optimization; Cambridge University Press: New York, 2004.
- ²⁵ Nocedal, J.; Wright, S. J. Numerical Optimization, 2nd Ed.; Springer: New York, 2006.
- ²⁶ Patel, P.; Wells, R. H.; Kaphan, D. M.; Delferro, M.; Skodje, R. T.; Liu, C. Computational Investigation of the Role of Active Site Heterogeneity for a Supported Organovanadium(III) Hydrogenation Catalyst. *ACS Catal.* **2021**, *11* (12), 7257–7269.
- ²⁷ Wells, R. H.; An, S.; Patel, P.; Liu, C.; Skodje, R. T. Single-Molecule Kinetics of Styrene Hydrogenation on Silica-Supported Vanadium: The Role of Disorder for Single-Atom Catalysts. *J. Phys. Chem. C* **2021**, *125* (37), 20286–20300.
- ²⁸ An, S.; Patel, P.; Liu, C.; Skodje, R. T. Computational Aspects of Single-Molecule Kinetics for Coupled Catalytic Cycles: A Spectral Analysis. *J. Phys. Chem. A* **2022**, *126* (23), 3783–3796.
- ²⁹ Da Silva, J. R. G.; Pinatti, D. G.; Anderson, C. E.; Rudee, M. L. A refinement of the structure of vitreous silica. *The Philosophical Magazine: J. Theor. Exp. and Appl. Phys.* **2006**, *31*, 713-717.
- ³⁰ Grimley, D. I.; Wright, A. C.; Sinclair, R. N. Neutron scattering from vitreous silica IV. Time-offlight diffraction. *J. Non-Cryst. Solids* **1990**, *119*, 49-64.
- ³¹ Mozzi, R. L.; Warren, B. E. The structure of vitreous silica. Journal of Applied Crystallography 1969, 2, 164-172.
- ³² Ewing, C. S.; Bhavsar, S.; Veser, G.; McCarthy, J. J.; Johnson, J. K. Accurate amorphous silica surface models from first-principles thermodynamics of surface dehydroxylation. *Langmuir* **2014**, *30*(18), 5133-5141.
- ³³ Fogarty, J. C.; Aktulga, H. M.; Grama, A. Y.; van Duin, A. C.; Pandit, S. A. A reactive molecular dynamics simulation of the silica-water interface. *J. Chem. Phys.* **2010**, 132, 174704.
- ³⁴ Grekov, D., Bouhoute, Y., Szeto, K.C., Merle, N., De Mallmann, A., Lefebvre, F., Lucas, C., Del Rosal, I., Maron, L., Gauvin, R.M. and Delevoye, L., Silica-supported tungsten neosilyl oxo precatalysts: Impact of the podality on activity and stability in olefin metathesis. *Organometallics* 2016 35(13), pp.2188-2196.
- ³⁵ Peters, B.; Scott, S. L. Single atom catalysts on amorphous supports: A quenched disorder perspective. *J. Chem. Phys.* **2015**, *142*, 104708.
- ³⁶ Vandervelden, C. A.; Khan, S. A.; Scott, S. L.; Peters, B. Site-averaged kinetics for catalysts on amorphous supports: an importance learning algorithm. *React. Chem. Eng.* **2020**, *5*, 77-86
- ³⁷ Khan, S. A.; Vandervelden, C. A.; Scott, S. L.; Peters, B. Grafting metal complexes onto amorphous supports: from elementary steps to catalyst site populations via kernel regression. *React. Chem. Eng.* **2020**, 5, 66-76.
- ³⁸ Sohn, H.; Camacho-Bunquin, J.; R. Langeslay, R.; Leon, P. A. I.; Niklas, J.; G. Poluektov, O.; Liu, C.; G. Connell, J.; Yang, D.; Kropf, J.; *et al.* Isolated, Well-Defined Organovanadium(Iii) on Silica: Single-Site Catalyst for Hydrogenation of Alkenes and Alkynes. *Chem. Commun.* **2017**, *53* (53), 7325–7328.
- ³⁹ Kaphan, D. M.; Ferrandon, M. S.; Langeslay, R. R.; Celik, G.; Wegener, E. C.; Liu, C.; Niklas, J.; Poluektov, O. G.; Delferro, M. Mechanistic Aspects of a Surface Organovanadium(III) Catalyst for Hydrocarbon Hydrogenation and Dehydrogenation. *ACS Catal.* **2019**, *9* (12), 11055–11066.
- ⁴⁰ Wells, R. H.; Skodje, R. T. Pathway-Switching Mechanism for Water-Catalyzed Ethanol Decomposition on Cu(111). *J. Phys. Chem. C* **2020**, *124* (17), 9385–9393.
- ⁴¹ Frisch, M. J.; Trucks, G. W.; Schlegel, H. B.; Scuseria, G. E.; Robb, M. A.; Cheeseman, J. R.; Scalmani, G.; Barone, V.; Petersson, G. A.; Nakatsuji, H. Gaussian 16 Rev. C. 01, Wallingford, CT. *Wallingford CT* **2016**.
- ⁴² Becke, A. D. Density-Functional Thermochemistry. III. The Role of Exact Exchange. *J. Chem. Phys.* **1993**, *98*, 5648-5652.
- ⁴³ Lee, C.; Yang, W.; Parr, R. G. Development of the Colle-Salvetti Correlation-Energy Formula into a Functional of the Electron Density. *Phys. Rev. B* **1988**, *37* (2), 785–789.
- ⁴⁴ Stevens, W. J.; Basch, H.; Krauss, M. Compact Effective Potentials and Efficient Shared-exponent Basis Sets for the First- and Second-row Atoms. *J. Chem. Phys.* **1984**, *81* (12), 6026–6033.
- ⁴⁵ Stevens, W. J.; Krauss, M.; Basch, H.; Jasien, P. G. Relativistic Compact Effective Potentials and Efficient, Shared-Exponent Basis Sets for the Third-, Fourth-, and Fifth-Row Atoms. *Can. J. Chem.* **1992**, *70* (2), 612–630.
- ⁴⁶ Cundari, T. R.; Stevens, W. J. Effective Core Potential Methods for the Lanthanides. *J. Chem. Phys.* **1993**, *98* (7), 5555–5565.
- ⁴⁷ Schäfer, A.; Huber, C.; Ahlrichs, R. Fully Optimized Contracted Gaussian Basis Sets of Triple Zeta Valence Quality for Atoms Li to Kr. *J. Chem. Phys.* **1994**, *100* (8), 5829–5835.
- ⁴⁸ Kozuch, S.; Shaik, S. A Combined Kinetic-Quantum Mechanical Model for Assessment of Catalytic Cycles: Application to Cross-Coupling and Heck Reactions. *J. Am. Chem. Soc.* **2006**, *128* (10), 3355–3365.
- ⁴⁹Kozuch, S.; Shaik, S. How to Conceptualize Catalytic Cycles? The Energetic Span Model. *Acc. Chem. Res.* **2011**, 44 (2), 101–110.
- ⁵⁰ Kozuch, S. A Refinement of Everyday Thinking: The Energetic Span Model for Kinetic Assessment of Catalytic Cycles. *WIREs Comput. Mol. Sci.* **2012**, *2* (5), 795–815.

⁵¹ Wodrich, M. D.; Sawatlon, B.; Solel, E.; Kozuch, S.; Corminboeuf, C. Activity-Based Screening of Homogeneous Catalysts through the Rapid Assessment of Theoretically Derived Turnover Frequencies. *ACS Catal.* **2019**, *9* (6), 5716–5725.

⁵² Saltelli, A.; Chan, K.; Scott, E. M. Sensitivity Analysis. Probability and Statistics; John Wiley & Sons: New York, 2009.

⁵³ Bai, S.; Davis, M. J.; Skodje, R. T. Sum over Histories Representation for Kinetic Sensitivity Analysis: How Chemical Pathways Change When Reaction Rate Coefficients Are Varied. *J. Phys. Chem. A* **2015**, *119* (45), 11039–11052

⁵⁴ Campbell, C. T. The Degree of Rate Control: A Powerful Tool for Catalysis Research. *ACS Catal.* **2017**, *7* (4), 2770–2779.

⁵⁵ Peters, B. Simple Model and Spectral Analysis for a Fluxional Catalyst: Intermediate Abundances, Pathway Fluxes, Rates, and Transients. *ACS Catal.* **2022**, *12* (13), 8038–8047.

⁵⁶ Byrd, R. H.; Hribar, M. E.; Nocedal, J. An Interior Point Algorithm for Large-Scale Nonlinear Programming. *SIAM J. Optim.* **1999**, *9* (4), 877–900.

⁵⁷ Campbell, C. T. Chlorine Promoters in Selective Ethylene Epoxidation over Ag(111): A Comparison with Ag(110). *J. Catal.* **1986**, *99* (1), 28–38.

⁵⁸ Linic, S.; Barteau, M. A. Control of Ethylene Epoxidation Selectivity by Surface Oxametallacycles. *J. Am. Chem. Soc.* **2003**, *125* (14), 4034–4035.

⁵⁹ Dasgupta, A.; He, H.; Gong, R.; Shang, S.-L.; Zimmerer, E. K.; Meyer, R. J.; Liu, Z.-K.; Janik, M. J.; Rioux, R. M. Atomic Control of Active-Site Ensembles in Ordered Alloys to Enhance Hydrogenation Selectivity. *Nat. Chem.* **2022**, *14* (5), 523–529.

⁶⁰ Medford, A. J.; Vojvodic, A.; Hummelshøj, J. S.; Voss, J.; Abild-Pedersen, F.; Studt, F.; Bligaard, T.; Nilsson, A.; Nørskov, J. K. From the Sabatier Principle to a Predictive Theory of Transition-Metal Heterogeneous Catalysis. *J. Catal.* **2015**, *328*, 36–42.

⁶¹ Michaelides, A.; Liu, Z.-P.; Zhang, C. J.; Alavi, A.; King, D. A.; Hu, P. Identification of General Linear Relationships between Activation Energies and Enthalpy Changes for Dissociation Reactions at Surfaces. *J. Am. Chem. Soc.* **2003**, *125* (13), 3704–3705.

⁶² Greeley, J.; Mavrikakis, M. Alloy Catalysts Designed from First Principles. *Nat. Mater.* **2004**, *3* (11), 810–815.

⁶³ Abild-Pedersen, F.; Greeley, J.; Studt, F.; Rossmeisl, J.; Munter, T. R.; Moses, P. G.; Skúlason, E.; Bligaard, T.; Nørskov, J. K. Scaling Properties of Adsorption Energies for Hydrogen-Containing Molecules on Transition-Metal Surfaces. *Phys. Rev. Lett.* **2007**, *99* (1), 016105.

⁶⁴ Logadottir, A.; Rod, T. H.; Nørskov, J. K.; Hammer, B.; Dahl, S.; Jacobsen, C. J. H. The Brønsted–Evans–Polanyi Relation and the Volcano Plot for Ammonia Synthesis over Transition Metal Catalysts. *J. Catal.* **2001**, *197* (2), 229–231.

⁶⁵ Zhao, Z.-J.; Liu, S.; Zha, S.; Cheng, D.; Studt, F.; Henkelman, G.; Gong, J. Theory-Guided Design of Catalytic Materials Using Scaling Relationships and Reactivity Descriptors. *Nat. Rev. Mater.* **2019**, *4* (12), 792–804.

⁶⁶ Vojvodic, A.; Nørskov, J. K. New Design Paradigm for Heterogeneous Catalysts. *Natl. Sci. Rev.* **2015**, *2* (2), 140–143.